TOPICAL COLLECTION: EUROSUPERALLOYS 2026

Miniature Mechanical Testing to Infer Damage from Accidental and Complex Thermal Exposure for Single Crystal Superalloys

YUANBO T. TANG, CASPAR SCHWALBE, JULIA BRUNTHALER,
ROGER C. REED, and SATOSHI UTADA

Mechanical testing featuring miniaturized specimens are resource-efficient alternative to standardized testing that can offer unparalleled insights. In this work, the established electro-thermal mechanical testing procedure was used for evaluating potential damage to microstructure given by unexpected thermal/mechanical load. Two conceptualized scenarios were considered. The first case concerns property deterioration given long-term complex exposure of temperature and stress, using specimens directly extracted from turbine blades. The second case concerns an 'accidental' solution treatment at near-incipient melting temperature. Quasi-static and dynamic tests were carried out to pick up potential property change against the reference condition. For the reference microstructure, low cycle fatigue was shown successful in yielding reproducible fatigue life and pick up location-dependent strain hardening response between suction *vs*. pressure side of a turbine blade. The property difference, given each scenario, was benchmarked accordingly and rationalized with microscopic evidence.

https://doi.org/10.1007/s11661-025-08096-6

I. INTRODUCTION

SUPERALLOY components are built to operate under extreme loading and thermal profiles. Their long-term safe operation is underpinned by high confidence life assessment, which requires accurate measurements of a range of properties, such as yield strength, low/high cycle fatigue, creep, notch sensitivity, and so on. The qualification testing constitutes a significant economic commitment of the alloy and process development.[1] As driven by the Net Zero 2050 vision, the current sustainability targets in the aerospace sector has made gradual change of the technological landscape.[2,3] Evidently, recovery, rejuvenation, and repair are playing an ever greater role in materials technology.[4–6] Alongside with full-scale standardized testing, alternative high-throughput testing featuring smaller-scale, even miniature specimens has gained strong traction that highlights resource efficiency.[7–9]

Various types of mechanical testing featuring miniaturized specimens have emerged in recent years, including the ones featuring methods based upon indentation,[10] tensile/compression,[11] punching,[12] or else bending/shearing.[13] Among them, an established miniature testing methodology known as electro-thermo-mechanical testing (ETMT) has been researched extensively[14] since its inception. The ETMT system conducts thermo-mechanical testing within an environmental chamber; in addition, it is designed to incorporate electrical resistivity measurements as a novel method for interpretation of microstructural evolution.[15] Given this unique feature, it has since been utilized creatively for various testing scenarios, such as high-throughput mechanical assessments,[8,16] tracking of recovery, recrystallization,[17] simulation of differential thermal contraction during investment casting,[18] damage assessment for component overheating,[19] and assessment of non-equilibrium microstructures,[20,21] to name a few.

The traditional view on miniaturized testing is that the data does not typically go beyond screening and ranking purposes—concerns over potential data scattering, cross-platform consistency, or else mismatching

---

YUANBO T. TANG is with the School of Metallurgy and Materials, University of Birmingham, Elms Road, Birmingham B15 2SE, UK and also with the Department of Materials, University of Oxford, Parks Road, Oxford OX1 3PH, UK. Contact e-mail: y.t.tang@bham.ac.uk CASPAR SCHWALBE and JULIA BRUNTHALER are with the MTU Aero Engines AG, Dachauer Str. 665, Munich, Germany. ROGER C. REED is with the Department of Materials, University of Oxford. SATOSHI UTADA is with the Department of Materials, University of Oxford and also with the Research Centre for Structural Materials, NIMS, 305-0047, 1-2-1 Sengen, Tsukuba, Ibaraki, Japan.
Manuscript submitted September 29, 2025; accepted December 22, 2025.

with full-scale standardized methods. Recent efforts have shown promises in this regard, where the ETMT results showed exceptional repeatability and consistency for quasi-static tensile compared with internationally recognized standards—American Society for Testing and Materials (ASTM)[22]—provided the caveats in measuring procedures are overcome. On the other hand, the ETMT approach has shown consistently a reduced creep rupture life compared to ASTM counterparts suggested by joule heating *via* electric current.[23]

This work will build upon the previously proven ETMT methodologies, where we conceptualized two novel testing scenarios. The case one simulates a series of complex thermal and mechanical exposure, which is representative during normal engine operation. The case two is to mimick 'an accidental thermal exposure' during solution treatment. Additionally, we extend the applicability of testing in two aspects—cyclic loading behavior and extraction of location-dependent properties from a thin cross-section in low pressure turbine blade. In each case, we benchmark against the standard microstructure as the reference, and we pinpoint and quantify the life debt and property deterioration for intentional thermal and/or mechanical loads to infer potential damage. Our findings successfully demonstrated pickup of static and dynamic property change subject to microstructural damage through thermal and/mechanical exposure.

II. EXPERIMENTAL METHODOLOGIES

A. *Materials*

Two batches of materials were used in the current study for case studies one and two, respectively. For case study one, the objective was to directly extract miniaturized specimens from low pressure turbine (LPT) blades with specific microstructure as a function of extraction location and thermal mechanical history. The approach aimed to compare property change from virgin blade versus blade after complex cycles of thermal and mechanical exposure. Two LPT blades were selected (Figure 1(a)) and sectioned at the same location (height and curvature) into sections of c.a. 50 mm × 16 mm × 5 mm (h,w,t). The virgin blade was fully heat treated with virgin microstructure. The second blade was fully heat treated and then subject to a series of complex thermal mechanical exposure on land mimicking in-service conditions. Thereafter, the condition is termed as 'pre-exposed.' The blade was made from SC2000 alloy with its nominal composition shown in Table I.[5] Inverse pole figure (IPF) results show the two materials have comparable [001] orientation alignment. Specimens were carefully extracted using wire-based electric discharge machining (EDM) with location information recorded, *i.e.,* on the suction side or pressure side, see cutting plan in Figure 1(b).

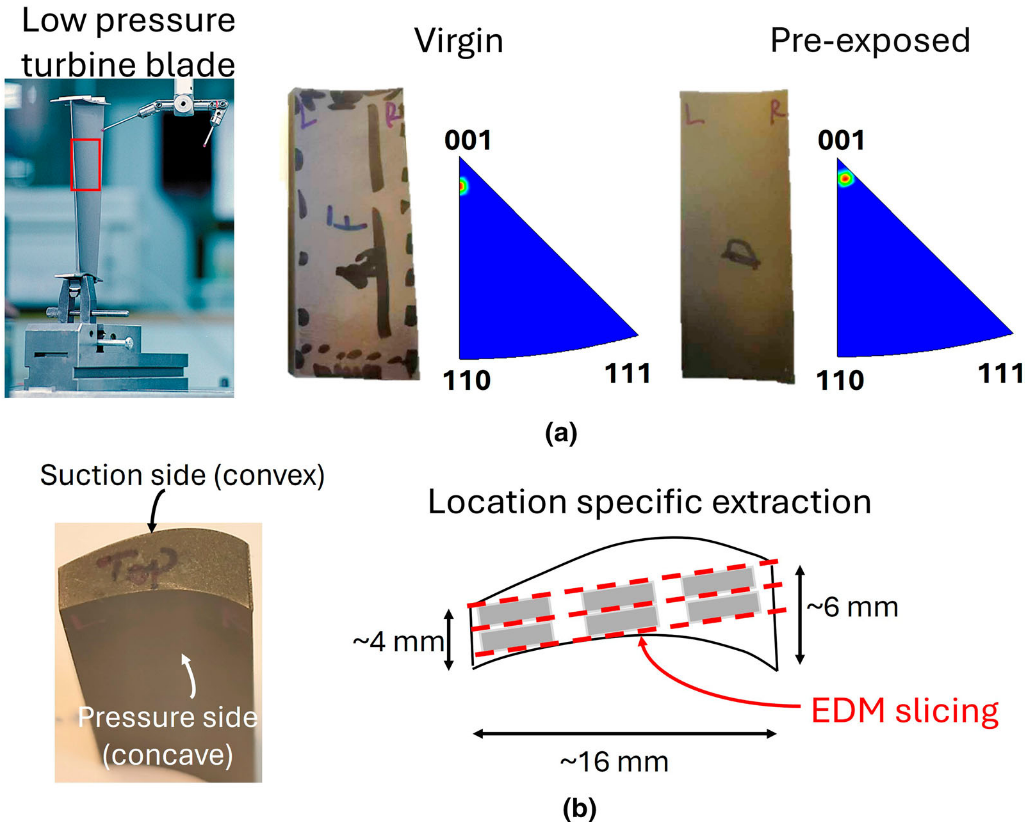

Fig. 1—(*a*) Photo of an example low pressure turbine blade and side view of blade section prior to final machining of miniaturized tests for virgin condition and after complex thermal mechanical exposure. Corresponding stereographic triangle showing alignment to 001 orientation. (*b*) Top view of the blade section prior to machining and electrical discharge machining plan showing the location specific extraction of specimens.

Table I. Nominal Compositions of Superalloys Used for Current Study in Wt Pct

	Ni	Cr	Co	Al	Ti	Ta	W	Mo	Hf	Zr	Re	C	B
Mar-M-247	Bal	8.4	10.0	5.5	1.0	3.0	10.0	0.7	1.5	0.05	—	0.15	0.015
SC2000	Bal	5.0	10.0	5.6	—	8.7	6.0	2.0	0.1	—	3.0	—	—

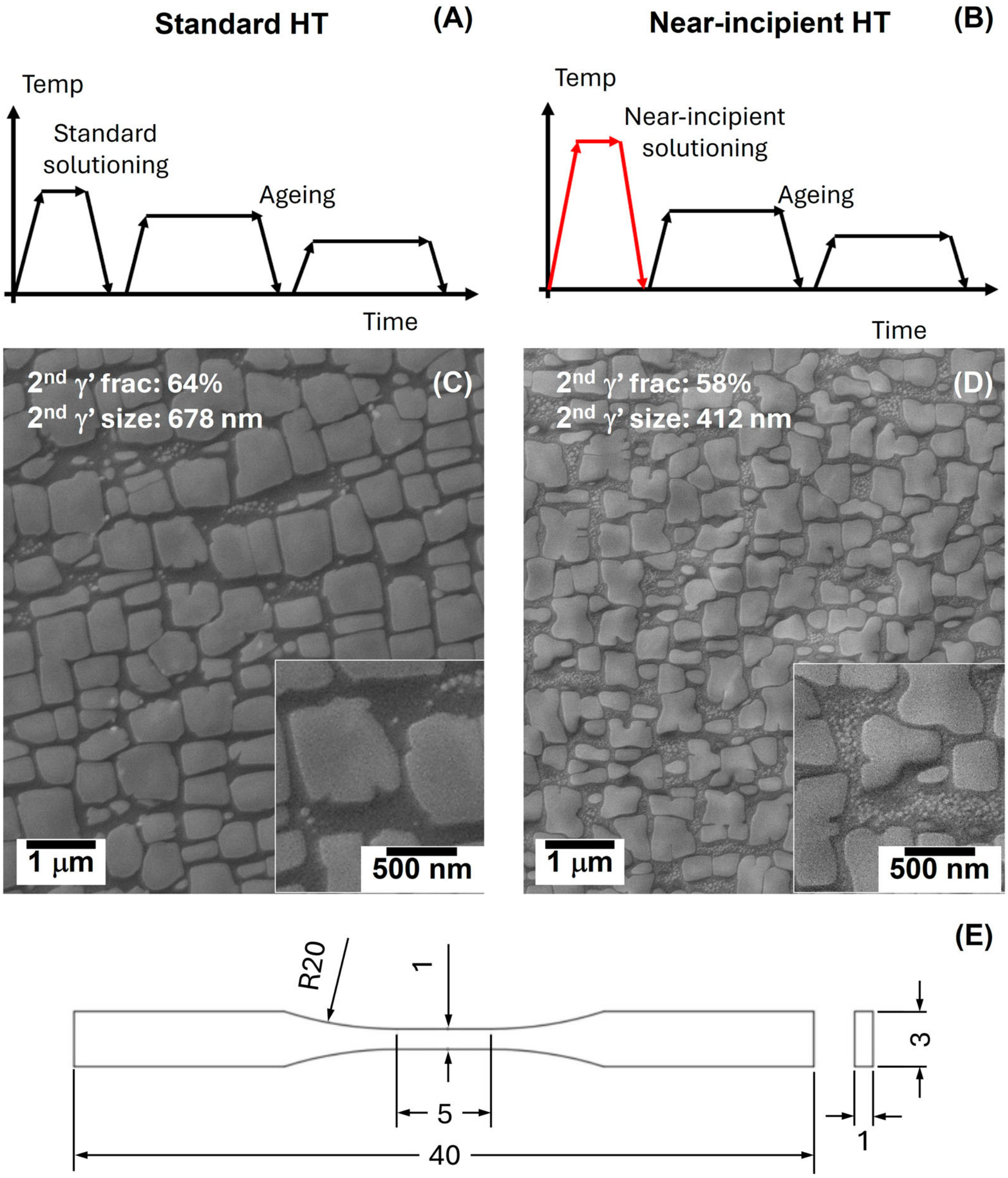

Fig. 2—Heat treatment schedule shown schematically for standard heat treatment (*a*) and near-incipient heat treatment (*b*). Typical γ/γ' microstructure for both treatments is shown in (*c*) and (*d*), respectively. Specimen geometry used for quasi-static and LCF test (*e*).

For case study two, the objective was to conduct LCF testing and to infer damage of the microstructure due to 'accidental solution treatment.' The control variable was the solution heat treatment temperatures, where an intentional near-incipient melting solution treatment was created to simulate 'accidental treatment' that is benchmarked by standard heat treatment. Mar-M-247 nickel-based single crystal superalloy was used for the study. The nominal composition of the material is shown in Table I. The single crystal material was received in bar form with the longitudinal orientation aligned with [001]. Both bars received had a diameter of 22 mm and a length of 90 mm. Two bars were received that came from the same casting, which were then

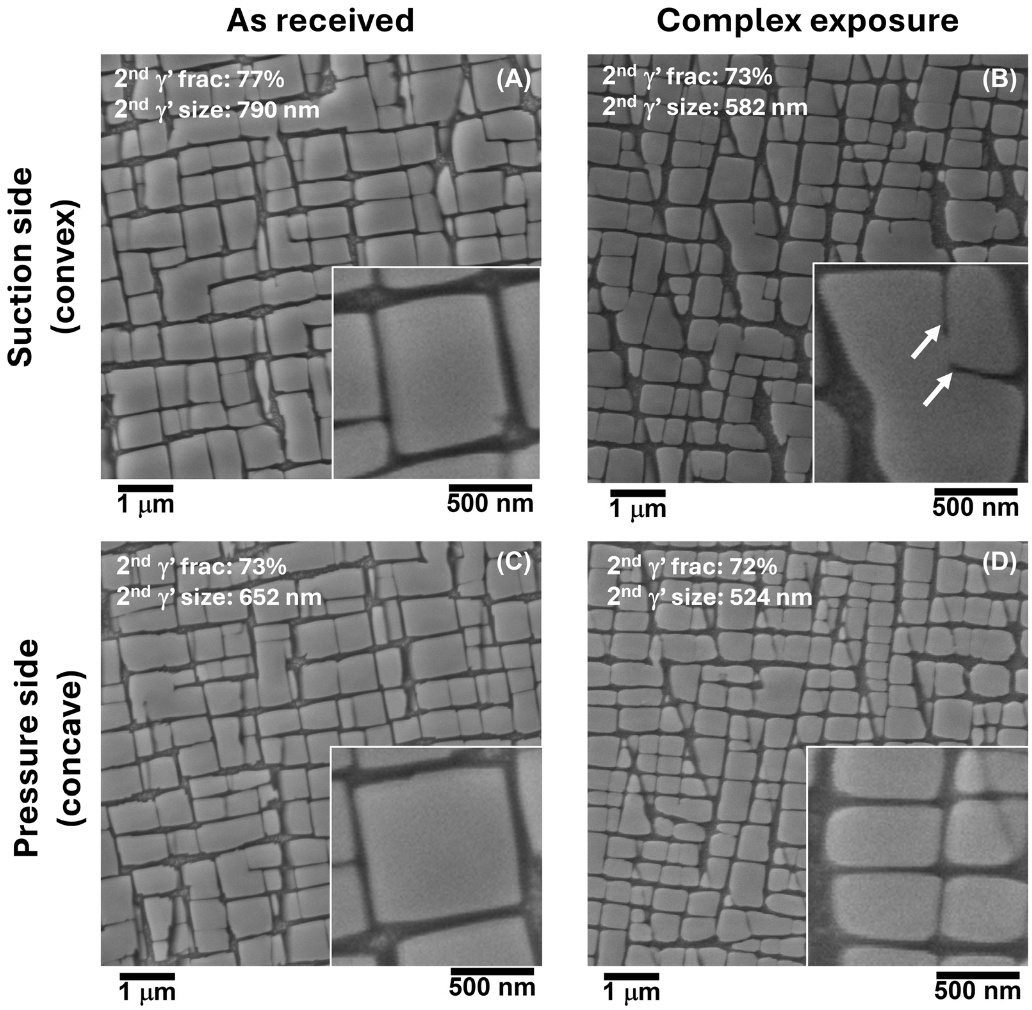

Fig. 3—Typical γ/*gamma*′ microstructure for virgin conditions (*a*), (*c*) *vs.* after complex thermal mechanical exposure (*b*), (*d*). The extraction location, i.e., suction side (a), (b) *vs.* pressure side (c), (d) for each condition is indicated. Each micrograph also shows a zoomed-in image to illustrate the morphology of γ/γ′ interfaces.

subject to different heat treatment, see a schematic illustration in Figures 2(a), (b). The ThermoCalc simulation with TCNI8 database suggests the solidus point is 1256 °C.[22] For the standard heat treatment, the solution temperature was achieved by step-wise increase with 1250°C as maximum temperature according to Reference 24. For the near-incipient melting treatment, the solution temperature was achieved by step-wise increase with 1290 °C as maximum temperature. Both solution treatment was held isothermally for 2 hours followed by double aging treatment according to Reference 25.

B. *Electro-thermo-Mechanical Testing (ETMT)*

Mechanical testing was conducted using an Instron electro-thermo-mechanical testing (ETMT) system. The specimens were extracted using wire-based EDM into geometries shown in Figure 2(e). This geometry was different from our previous work;[22] it features a smooth transition between the gauge to non-gauge sections with a fillet radius of 20 mm and hence reducing stress concentration during the LCF testing. The same sample geometry was used for all tests including uniaxial tensile. All specimens were grounded using abrasive media up to 4000 grits prior to testing.

Static tensile tests were conducted at a strain rate of 10^{-4} s^{-1} at room temperature for both case one and two. Speckle patterns were applied on the specimen surface to allow for tracking of deformation. This is achieved using VHT flame proof high-temperature paint, using white primer as the background and sprayed with scattered black paint as tracking speckles. Strain measurement was conducted by Imetrum video extensometry. The virtual gauge mark was set with an area of approximately 1 × 1 mm^2, and the gauge length was set at 5 mm for RT test. The frame rate was set at 2 Hz. 1050 °C tests were conducted on specimens in case study two. Heating was delivered by DC current where the flat end grips were water cooled.[8] Temperature was measured using type R thermocouple which was spot welded onto the side of the specimen. A temperature gradient is therefore established which can be approximated as a parabolic profile along the loading

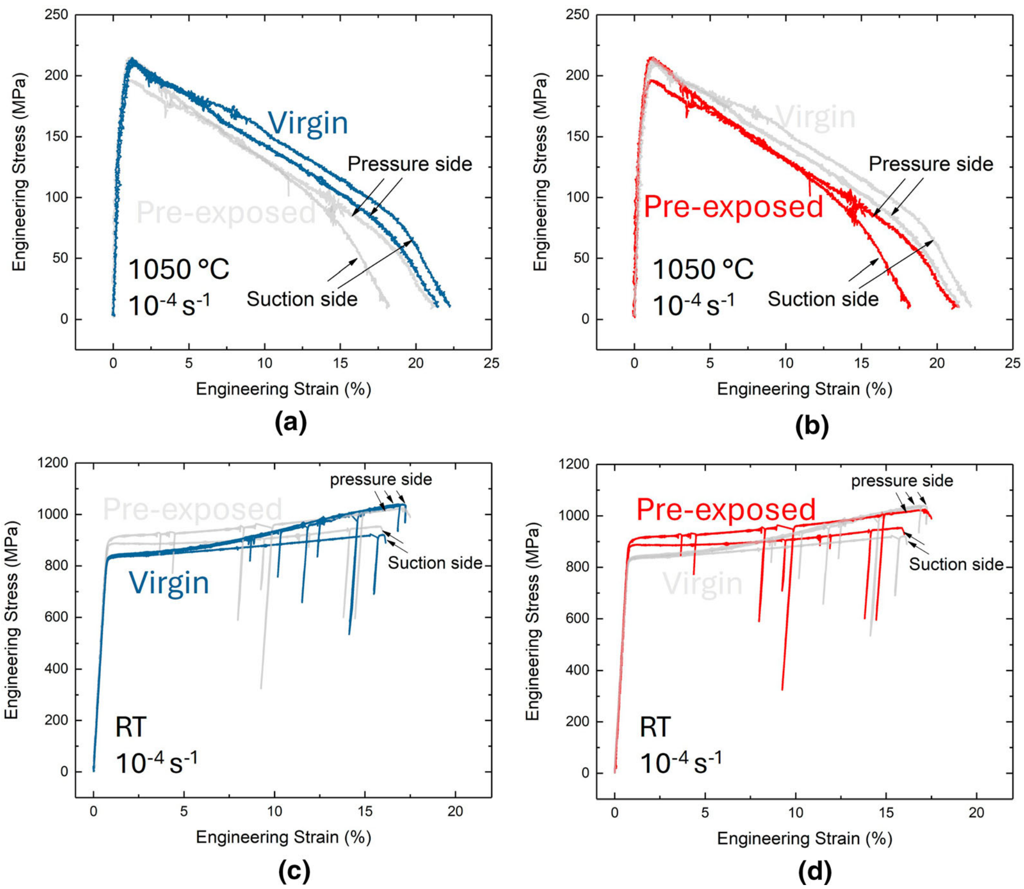

Fig. 4—Engineering stress–strain curves for [001] single crystal measured at 1050 °C (*a*), (*b*) and room temperature (*c*), (*d*). The specimens measured were distinguished by the conditions for virgin (a), (c) and after complex thermal mechanical exposure (b), (d), where the sample extraction location, suction side *vs*. pressure side, is annotated in the curve, too.

direction.[8,26] The central ~3 mm is shown to obtain an equilibrium temperature distribution; thus, the virtual gauge length was set at 3 mm for the high-temperature tests conducted.[14] In order to account for potential parasitic voltage, the DC current was reversed by changing circuit directions. The strain rate conducted was also 10^{-4} s^{-1} and strain was measured by video extensometry within the central 3 mm for elevated testing. Further analysis on strain mapping was conducted using MATLAB-based open source software 'Ncorr,' with detailed procedure provided elsewhere.[27] It is worth noting that the Joule effect heating can potentially cause a change, usually an acceleration, in the kinetics of phase transformation, recrystallization or deformation[23,28] *via* electroplasticity or electromigration, especially for a long hold. It is, however, unlikely to impose a significant effect during the relatively short tests carried out in the present study.[22]

Dynamic testing was conducted in load-controlled mode. A strain-controlled fatigue tests was not possible in the system used as the video extensometry capture rate at 10 Hz was not sufficiently high to be used as a control channel. LCF tests were carried out for samples in case study two under triangular waveform. Time taken for the maximum and minimum stresses each takes 1 s with no dwell, therefore stress frequency was 0.5 Hz. The stress ratio (R), *i.e.,* max/min stress, was set as 0.1. The set max stress values were 900, 950, and 980 MPa, respectively, yet the applied stress was used as the actual stress level recorded by the load cell. A linear variable differential transformer (LVDT) was used to monitor travel between the cross heads.

C. *Scanning Electron Microscope*

Electron microscopy samples were prepared using standard metallography route using serial grinding and polishing. The final step was finished using 40 nm colloidal silica suspension for 5 mins in most imaging conditions. γ' size measurements were carried out with samples subject to electrolytic etching by applying for a 3V potential difference in 10 pct H_3PO_4 solution. γ' precipitation imaging was conducted using a Zeiss Crossbeam 540 field emission gun scanning electron microscope (FEG-SEM). A secondary electron detector was used to probe the γ/γ' boundary at 15 kV acceleration voltage and a probe current of 1 nA.

Quantitative analysis of fraction and size distribution of the precipitate was conducted using ImageJ software.[29] Necessary background smoothing function and binarization based upon histogram were applied to distinguish γ' precipitates from the matrix. γ' fraction

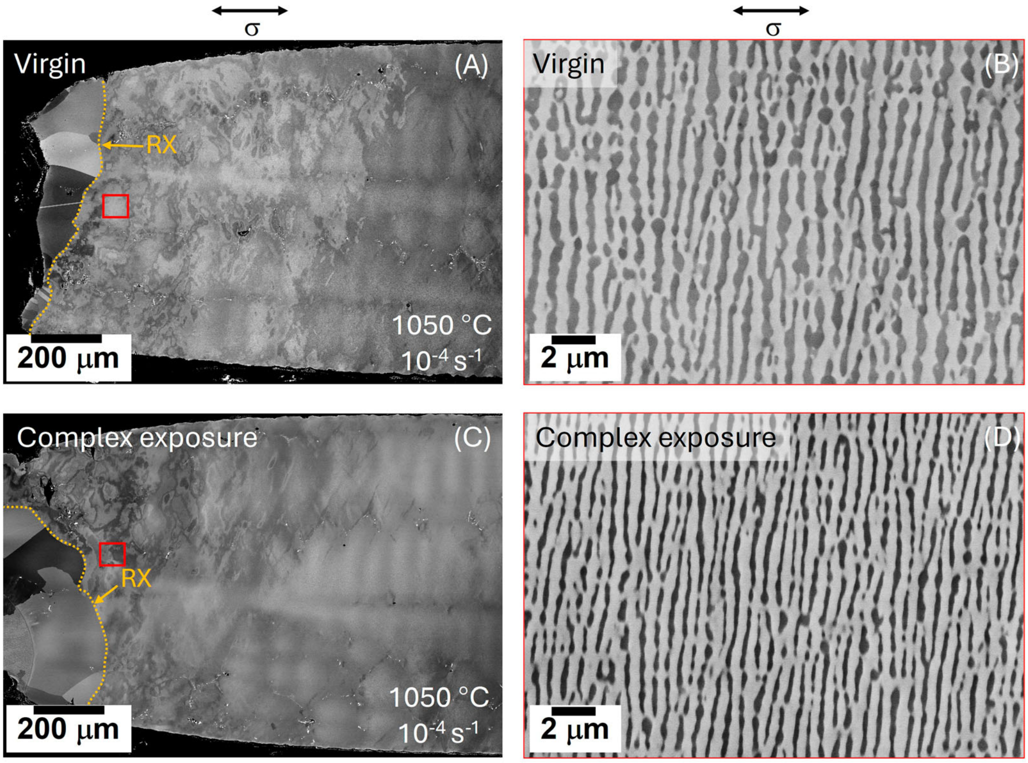

Fig. 5—Fractured sample tested at 1050 °C for virgin (*a*), (*b*) and pre-exposed (*c*), (*d*) conditions. Zoomed-in micrographs of rafted microstructure are shown in (b), (d).

and size analyses were conducted for the dendrite core region in all cases using representative area of at least 100 μm^2. Electron backscattered diffraction (EBSD) mapping was carried out using EDAX DigiView5 detector in a Zeiss Gemini300 FEG-SEM system. EBSD pattern quality was recorded as 120 × 160 resolution with a step size of 0.1 μm. Collected EBSD indexed data were postprocessed using EDAX OIM analysis*TM* 8. Electron channeling contrast imaging (ECCI) was employed using a Zeiss Gemini300 FEG-SEM system at 20 kV acceleration voltage and an angular selective backscatter detector with a small stage tilt (~ 5°).

III. RESULTS AND DISCUSSIONS

A. *Case One: Location-Dependent Property Extraction Subject to Complex Exposure*

1. *Microstructure*

Typical microstructure revealing size and distribution of γ' is shown in Figure 3. On the suction side of the blade (convex curvature), the distribution of γ' for virgin and complex exposed case is shown in Figures 3(a), (b), where for the pressure side, counterpart (concave curvature) is shown in Figures 3(c), (d). For the virgin case, the secondary γ' fraction is measured at 77 pct with an average side length of 790 nm (assuming perfectly cubic) for the suction side, whereas for the pressure side, the fraction was 73 pct and average side length was 652 nm. The size difference between the two is noticeable despite not excessive. The location-dependent microstructure is considered to originate from the complex geometry of the blade which does not experience a homogeneous heat transfer in all locations arising from solidification or subsequent homogenization treatment. The different cooling rates from near or above the γ' solvus temperature are known to alter γ' distribution.[30] For the complex exposure case, the suction side microstructure also obtains marginally larger precipitate size than the pressure side: 582 *vs.* 524 nm. The volume fraction remained similar at 73 and 72 pct, respectively.

The precipitation size reduction in the pre-exposed case is significant, which is consistently observed regardless of their location found in the blade. The average precipitate size reduced from 790 to 582 nm for the suction side and reduced from 652 to 524 nm for the pressure side. A plausible explanation is that inverse coarsening has assisted this evolution,[31,32] where large precipitates split into smaller ones driven by elastic stresses at the interface as it experiences thermal exposure. Figure 3(b) provides evidence for this, see annotated arrows, where a large cubic precipitate was in process of splitting into smaller ones.

The morphology of γ' precipitate in the virgin microstructure is highly cuboidal with sharp corners and flat boundaries, which is typical of single crystal superalloy with a large lattice misfit.[33] The morphology has since changed when that were exposed of thermal and mechanical loads, see Figures 3(b), (d), the corners of the precipitates show rounded features and non-sharp edges. The rounded features suggest a change, typically a reduction in the lattice misfit due to local

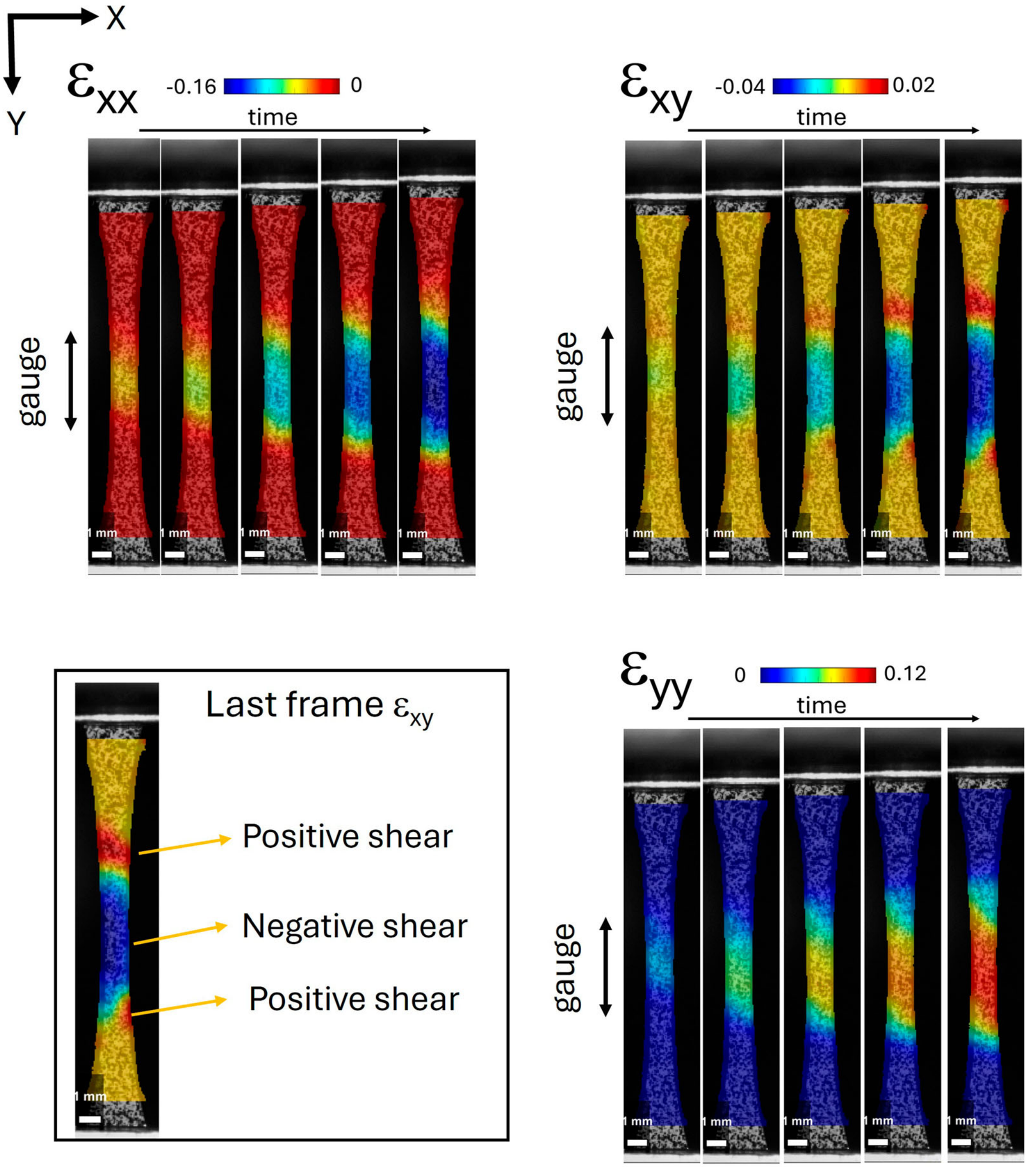

Fig. 6—2D strain tensor of a specimen under quasi-static uniaxial tension at five time intervals. Strain revealed in horizontal direction (ε_{xx}), vertical direction (ε_{yy}) and in shear (ε_{xy}). Bottom left shows the last frame of shear with annotated shear signs.

compositional rearrangement that is facilitated with defects, such as dislocations at the interface.[34] Further exposure, especially at higher temperature (over 1000 °C), could promote the formation directional coarsening (rafting).

2. *Elevated temperature deformation and rafting*

The high-temperature deformation is shown in Figures 4(a), (b). For the virgin microstructure, the stress–strain curves seem insensitive to location, where the pressure and suction side samples have their curves overlapped. Similarly, the pre-exposed specimens also obtained comparable stress–strain curves, see Figure 4(b). All samples showed a similar strain softening behavior postyielding. For avoidance of doubt, similar strain softening is observed for tensile testing at elevated temperatures using conventional furnace with standard specimen geometries,[10,22] which is attributed to creep strain relaxation instead of overheating due to an early necking—with the aid of DIC, the necking was found only at near the rupture point. Despite a slightly lower stress (c.a. 15 MPa) observed in the pressure side specimen, it is within the level of measuring uncertainty at elevated temperatures, especially at a temperature over 1000 °C where microstructure is highly sensitive to temperature uncertainty. Therefore, we conclude no notable difference in strength that was observed at 1050 °C in between the virgin *vs*. pre-exposed specimens regardless of sample extraction location. In addition, despite a possibility of a small compositional difference might incur from the two blades as they were produced from different melts. The highly comparable tensile behavior suggests the potential difference in composition is negligible.

The post-mortem analysis, however, has shown intriguing insights between virgin and pre-exposed samples. Figure 5(a), (c) shows the fracture tip of specimens of both conditions tested at 1050 °C. Both revealed the fracture tip was associated with recrystallization, which is expected given a significant fracture strain of c.a. 20 pct at 1050 °C. Given the presence of necking, the actual temperature might be higher than this value due to a higher current density at the necking region, which further facilitated the recrystallization event observed.

Furthermore, directional coarsening, the so-called rafting effect was observed for all samples close to the fracture tip. The γ' phase was originally cuboidal which now has become continuous that is perpendicular to tensile loading. Although more frequently observed in the crept samples, it is not surprising it arises for specimens deformed at a slow strain rate at 1050 °C. In the two cases shown, the rafted γ' stripes (dark contrast) are coarsened perpendicular along the tensile axis.

The degree of rafting is analyzed using the rafting parameter R to describe the extent of this evolution, as proposed by Ignat *et al.*[35] For a given area, then rafting parameter R is defined as

$$R = L/2T$$

where L is the average length of the precipitate and T is the average thickness. Thereby, for an idealized unrafted microstructure, the R value equals to 0.5. The increase of R value suggests an increased extent of rafting. In our analysis, we have utilized ImageJ software in producing Feret diameters of each isolated γ' strip. For estimation, Feret maximum (or Feret diameter) is taken as L and Feret minimum is taken as T. We conducted the evaluation of 400 μm^2 per microstructure. The rafting parameter $R_v = 2.5$ and $R_{exp} = 3.2$ (subscript v for virgin microstructure and exp for pre-exposed). The γ' fraction for the virgin and pre-exposed samples is 0.42 and 0.32, respectively, in the rafted region. Both microstructures have experience appreciable rafting, where the exposed sample shows a higher magnitude compared to the virgin counterpart. The rafting kinetics is facilitated by the reduction of γ/γ' coherency and a relaxation of interfacial misfit, which tendency the exposed microstructure has shown even prior to the loading, recap Figure 3. The difference in the γ' fraction of the rafted microstructure might also be attributed to potentially a higher temperature during the final stage of deformation when necking has occurred. Nonetheless, the comparable tensile yielding response at 1050 °C suggests the degree of rafting is unlikely to make a significant contribution in strengthening response.

3. *Room-temperature deformation and load drop phenomenon*

Figure 4(c), (d) shows engineering stress–strain curves tested for both microstructure at room temperature and 1050 °C, where sample extraction locations, *i.e.,* suction *vs.* pressure side, are annotated. The virgin microstructure, see Figure 4 (c), shows a consistent yield strength of 837 MPa for both suction and pressure side specimens. However, a difference in work hardening behavior is observed. The pressure side specimens consistently demonstrated a stronger work hardening response and achieve a higher UTS of 1040 MPa compared to the suction side (923 MPa). The pre-exposed sample (d), by contrast, shows higher yield strengths of 884 MPa (suction) and 904 MPa (pressure). An increase in yield is likely contributed by their smaller precipitate size. Once again, the pressure side specimen demonstrates a higher UTS of 1021 MPa compared to the suction side (950 MPa).

An intriguing load drop phenomenon was revealed in all tensile curves at room temperature. As the deformation progresses, there were multiple events of sudden drop of engineering stress which is followed by rapid recovery. This has been consistently observed for all samples in case study two as well, in total 10 specimens, therefore unlikely to be isolated events such as sample slipping. On the macroscopic level, Figure 6 shows the 2D strain tensor of the deformation process for pre-exposed (suction side) sample at room temperature at five different strain intervals until global strain reaches 14 pct. The ε_{xx}, ε_{yy} , and ε_{xy} maps illustrate deformation occurring in horizontal, vertical, and shear, respectively. As a reference, the gauge section is also indicated. As the

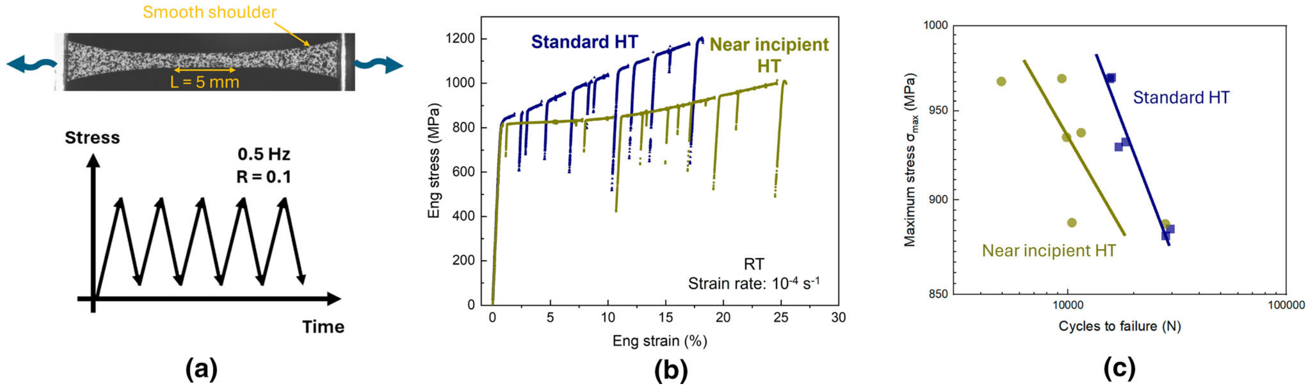

Fig. 7—(*a*) Example of a speckled specimen under loading (horizontally) and loading profile of 0.5 Hz and R =,0.1. (*b*) Typical engineering stress-strain curves for standard and near-incipient heat treatment at room temperature. (*c*) Fatigue cycle to failure of each heat treatment condition plotted against maximum stress applied.

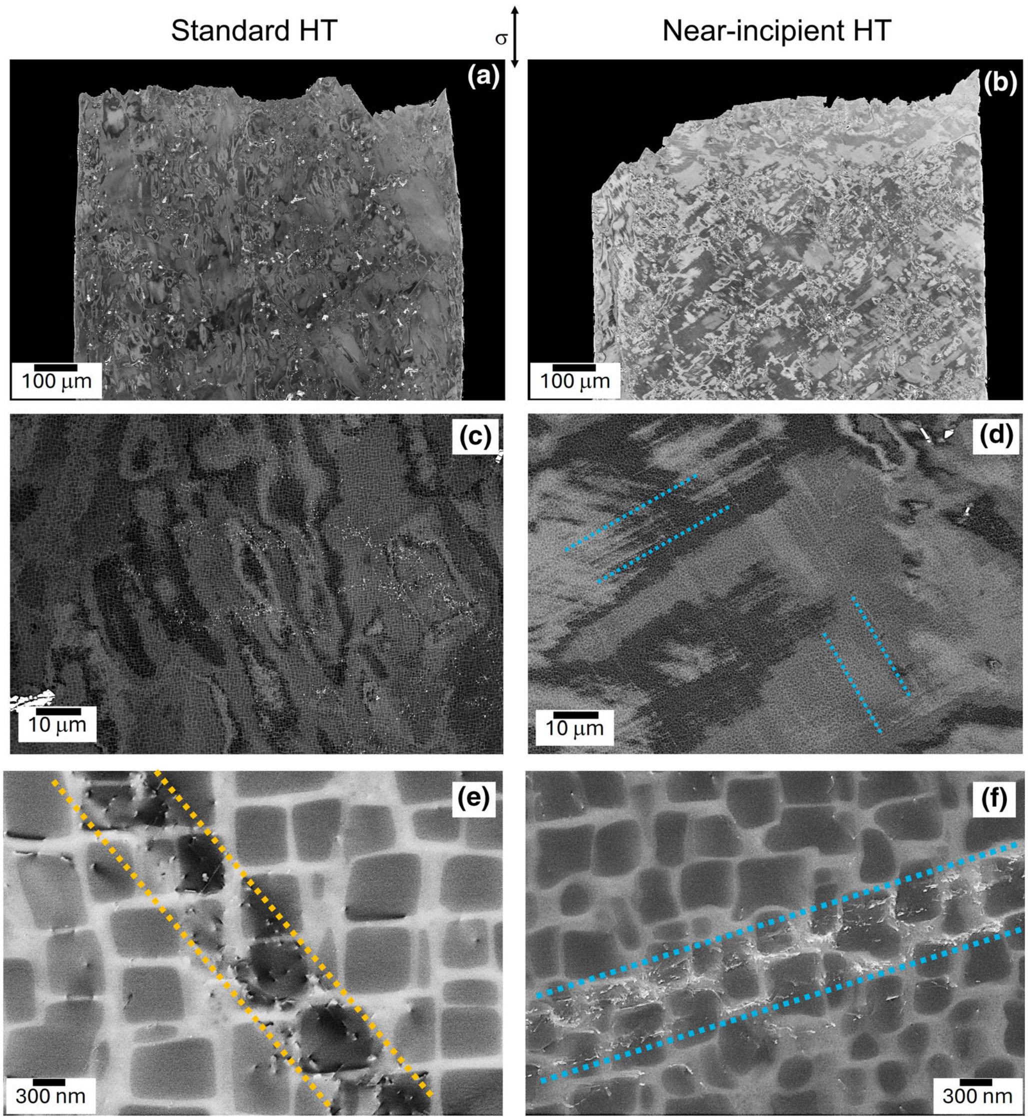

Fig. 8—Backscattered electron imaging at two magnifications and electron channeling contrast imaging (ECCI) showing typical dislocation structures within the γ/γ' microstructure in shear bands for standard (*a*), (*c*), (*e*) and near-incipient heat treatment (*b*), (*d*), (*f*).

Table II. LCF Cycle to Failure for Standard HT and Near-Incipient HT

Materials	Set Stress	Measured Stress	Cycles to Failure (Nf)	Average Nf
	MPa	MPa		
Standard HT	900	884	29421	28730
	900	881	28039	
	950	932	19376	18211
	950	930	17046	
	980	969	15539	15695
	980	969	15851	
Near-incipient HT	900	887	27882	19150
	900	888	10417	
	950	938	11480	10662
	950	935	9844	
	980	967	4951	7160
	980	969	9369	

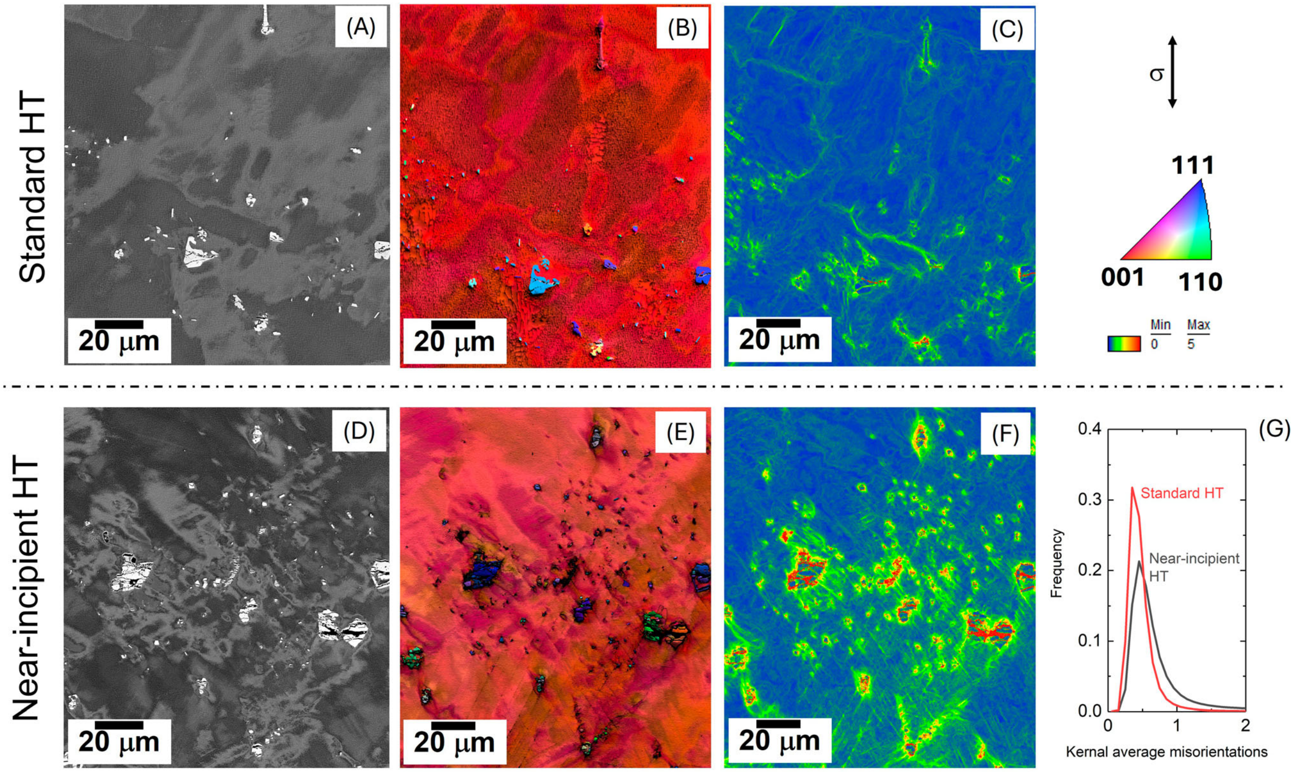

Fig. 9—The BSE SEM near carbides, inverse pole figure map and Kernal average misorientation (KAM) map near fracture tip of LCF samples tested at 980 MPa for standard treated (*a*) through (*c*) and near-incipient treated (*d*) through (*f*). Histogram of the KAM map is shown in (*g*).

deformation progresses, the near-incipient case shows a relatively flat region where strain hardening is minimal, it is indicative that deformation was initially localized and then gradually propagated to achieve homogeneity, resembles the 'Lüders band' like deformation, despite without a distinctive drop in stress.[36,37] This is supported by the DIC evidence as shown in Figure 6, where plasticity onset was indeed a localized (first frame) to a region much smaller than the gauge, which then propagated homogeneously across the entire gauge.

The ε_{xy} shear, however, shows an interesting feature, where both positive and negative shear strain is observed at the same sample throughout the deformation. Even when the specimen was initially deformed, a small shear strain was detected to develop in the gauge due to lattice rotation. Simultaneously, an opposite sign shear is observable at above and below the deformed region even at small level of deformation. The fixed ends are physical constraints to local lattice rotation, as if the specimen is 'fighting the grips.' As deformation proceeds, the gauge volume will work harden and achieve a higher yield strength compared to the non-gauge part. For a gradual transition in dog bone shoulder (large fillet radius), such as the case studied here, the non-gauge part would undergo some deformation. Therefore, as shown in the ε_{xy} shear map, when two opposite and concurrent lattice rotations are in action, plastic instability could be promoted and causes rapid elastic recovery due to countering rotation. This is considered one potential cause to the macroscopically observed load drop and its immediate recovery. For single crystal materials, load drop phenomenon is often reported in much smaller scales, such as compression of micro-pillars, and often attributed to dislocation bursts or avalanche.[38,39] It is, however, rarely reported for bulk specimens with a cross-section on the order of mm^2, especially the load drop was significant and consistently observed. It could be associated with the burst of planar faults within γ' instead of dislocations in the γ channels, those are of higher energy penalty and more likely to induce a response on the meso/macroscopic scale. Lastly, it is interesting to note that the load drop phenomenon is only observed in the current sample geometries, and not observed previously for similar single crystal superalloys when tested under a much sharper fillet transition.[22] Hence, it is considered sensitive to the gripping constraints, and the fillet radius.

B. *Case Two: Accidental Thermal Load*

1. *Microstructure*

A typical γ/γ' microstructure after standard HT is shown in Figure 2(c). The secondary γ' precipitate is measured as 64 pct in volume fraction with very occasional occurrence of tertiary γ' found in γ channels. The precipitates exhibit a cuboidal morphology, and the average side length is 678 nm assuming precipitates are perfectly cubic. The near-incipient HT counterpart showed a reduced volume fraction of 58 pct in secondary precipitates, where the morphology also changed

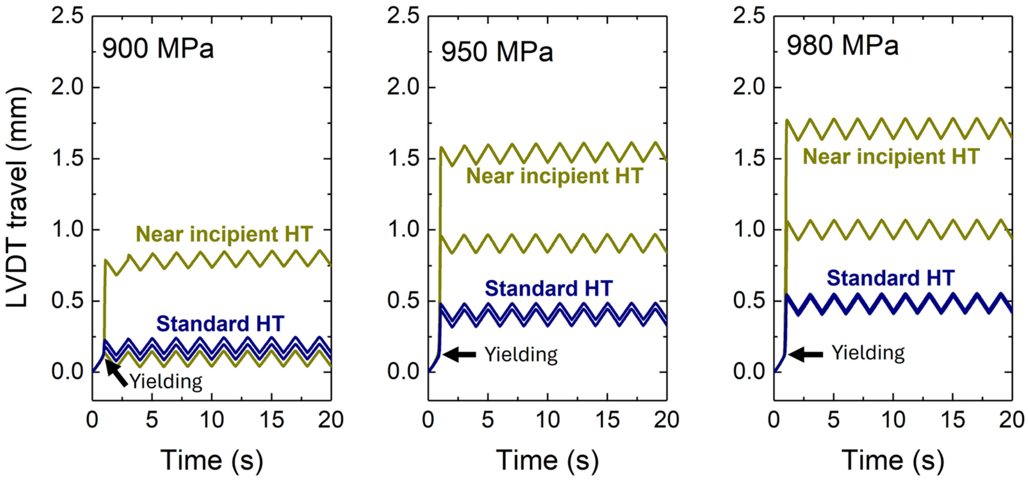

Fig. 10—The LVDT travel of fatigue samples at a stress level from 900 to 980 MPa for the initial 10 cycles for both heat treatments.

from cuboidal to octodendritic demonstrating signs of splitting up. The average γ' size has reduced to 412 nm. On the other hand, tertiary γ' occurrence is much more frequent in γ channels, which is likely formed during cooling and subsequent aging.

2. *Shear banding in quasi-static tensile*

The engineering stress-strain curves for each microstructure is shown in Figure 7 (b). Both standard and near-incipient HT samples obtained a comparable yield strength of 804 and 806 MPa, respectively. The work hardening behavior, however, is significantly different between the two. The near-incipient melting case showed a plateau of stress up to approximately 10 pct engineering strain with a gradual work hardening afterward until fracture at 25 pct that reached an ultimate tensile strength (UTS) of 1013 MPa. By contrast, the standard HT case demonstrated a strong hardening response after yielding. The plastic regime shows a near-linear work hardening until it fractures at 18 pct with the UTS of 1204 MPa. In avoidance of doubt, the standard HT obtained in the current study is different from our previous study,[22] which results indifferent work hardening behavior.

Microscopically, the two microstructures have shown different tendencies of developing shear banding. As shown in Figure 8, microscopic shear bands of the fractured specimens subject to quasi-static tensile can be found in the standard microstructure but much less frequently compared to the near-incipient HT sample. Examples of higher magnification images are shown in Figures 8(c), (d). It is apparent that shear banding is more frequently observed in the near-incipient case, which attributes to more sites of strain localization that would adversely affect the fatigue behavior. ECCI imaging of some shear bands is shown in Figures 8(e), (f). The bands are shown as intense localization of dislocations and/or faults with a width that is just below one micrometer. Although it is challenging to determine the exact crystal defects using ECCI alone, such as dislocations and planar defects like anti-phase boundary (APB) and different types of stacking faults,[40] their occurrence can be assumed given their location according to the well-established References 41, 42, *i.e.,* dislocations in γ matrix channels and planar faults within γ'.

For the standard HT microstructure in Figure 8(e), dislocations and faults do not show a strong tendency toward locations – they were frequently found both in γ channels and within γ' precipitates. However, for the near-incipient HT case, see Figure 8(f), dislocations and faults are primarily observed within the γ channels and less associated within the γ' precipitates. The differential behavior agrees with the work hardening rates observed. Shearing stress required of γ' precipitates *via* stacking faults and/or APB is considerable, where order hardening promotes a stronger work hardening response for the standard HT case in comparison with piling up of dislocations at γ channels in the near-incipient HT case. Given a distinctive γ' morphology, distribution and fraction between the two cases, it is speculated that a level of compositional variation in γ' precipitates exists, which the APB energy is sensitive to and thereby affected the work hardening rates observed.

3. *Low cycle fatigue*

The cycles to failure plot for standard and near-incipient HT are shown in Figure 7(c), where the fatigue life data are shown in Table II. The maximum stresses are plotted as measured rather than set stress. The standard HT specimens has shown good reproducibility of cycles to failure. At each stress level, two tests were performed and both specimens exhibited very similar fracture cycles, see Table II. The variation in cycles to failure between the repeats is not more than 8 pct in the worst case. The trend line plotted suggested a linear relationship for max stress to the logarithmic of cycles to failure. The excellent reproducibility of LCF results suggests the testing procedure applied is sufficiently robust as well as the homogeneity of standard HT microstructure is satisfactory.

On the contrary, the near-incipient HT demonstrates a large level of scatter in cycles to failure. The trend line is plotted based upon the average values at each stress level. At the set stress of 900 MPa, the two specimens failed at 10417 and 27882 cycles, respectively, differed by a factor of 2.7 time. Similarly at the set stress level of 980 MPa, specimens failed at 4951 and 9369 cycles, respectively, demonstrate a variation of 1.9 times. Compared to the standard HT case, not only a large scatter is seen in the LCF life for the near-incipient HT, it also shows a markedly reduced cycles to failure. For instance, the average failure cycle reduced from 28730 to 19149 at the lowest stress level and from 15695 to 7160 at the highest stress level. The fatigue life reduction was 33, 41, and 54 pct at max stresses are 900, 950, and 980 MPa, respectively.

The reduction of fatigue life is considered caused by the very different work hardening behaviors coming from the two HTs. In the case of a fix load, materials with higher work hardening rate will be strained to a lower strain level during the first cycle. The difference in the initial plasticity that took place can be considerable. For the given stress-strain curves in Figure 7(b), the first cycle would produce an engineering strain of ~4pct in the standard HT case, which it would be of ~16 pct in the case of near-incipient HT. The large pre-strain would have induced large density of dislocations and planar faults, which might already caused some hard particles to fracture, such as MC carbides, and thereby increase the number of fatigue initiation sites. Figure 9 shows SEM, IPF and Kernal average misorientation (KAM) map near the fatigue fracture in each case. The KAM histogram (g) demonstrates that the a massively increased local lattice misorientation observed in the near-incipient case, attributed to remnant of pre-deformation during the first fatigue cycle. This is particularly intense in the vicinity of carbides. Eventually, the irreversible damage has affected subsequently fatigue propagation through dislocation and particle fracture, which leads to a considerable fatigue debit in the near-incipient case.

The varied work hardening behavior between the two microstructures is considered to originate from the γ' size and distribution. The near-incipient HT case has a bimodal γ' distribution, and the mean size of secondary γ' is 412 nm with appreciable tertiary precipitates. In contrast, the standard HT case has a predominately unimodal distribution with only sparsely distributed tertiary γ'. The increased work hardening response in the unimodal coarse-γ' has been consistently observed elsewhere, such as in RR1000.[43] The increased Orowan looping and cross slipping activities around the larger precipitates are associated with the observed hardening behavior.

The scatter of LCF is discussed next. Since the work hardening rate in the near-incipient case is low, it is hence more prone to have a substantial deformation during the first fatigue cycle at a given stress. To visualize the pre-deformation of each specimen, the cross-head travel distance is used as a proxy for the initial ten LCF cycles of all testing conditions as shown in Figure 10. Clearly, for the standard HT case, the level of initial deformation is highly similar to each other, which gave reproducible LCF life. In contrast, the near-incipient HT case experienced a vastly different level of plasticity after the initial loading. The scatter in the initial plasticity suggests a varied level of crack initiation sites that lead to LCF response. In addition, the markedly different initial deformation manifests inconsistent work hardening response in each sample, suggesting the microstructure in the near-incipient case would show a degree of heterogeneity.

IV. SUMMARY AND CONCLUSION

In this work, we highlight the use of ETMT miniature testing as an alternative to standardized testing for two conceptualized scenarios. It has shown potential in gaining insights with excellent consistency in probing location-dependent properties from components and dynamic properties. The following specific conclusions can be drawn.

1. Miniaturized specimens extracted from the suction and pressure side of virgin low pressure turbine blades demonstrated similar yield strength at room temperature and 1050 °C. However, the suction side shows more pronounced work hardening behavior than the pressure side at room temperature.
2. Specimens after complex thermal–mechanical exposure demonstrates a higher yield strength at room temperature, which is considered due to their finer precipitation sizes obtained from inverse coarsening. No significant differences observed for high-temperature testing at 1050 °C between the two microstructures with/without the exposure, despite a much greater extent of rafting observed in the exposed condition.
3. The near-incipient case showed similar yield strength compared to the standard case. However, the near-incipient case shows a significantly reduced work hardening rate and ultimate tensile strength in comparison. This is attributed to change of secondary precipitates morphology from cuboidal to octodendritic with a reduction in size and volume fraction yet an increased occurrence of tertiary precipitates.
4. The LCF behavior for the standard heat treatment shows excellent repeatability from all stress ranges tested, suggesting robust consistency of the miniaturized dynamic testing procedure. The near-incipient case, however, showed markedly reduced average fatigue life and significantly large scatter in fatigue life.

ACKNOWLEDGMENTS

The authors are grateful for MTU Aero Engines AG (Germany) for provision of materials used in this study and for the insightful technical discussions with Dr Thomas Göhler.

CONFLICT OF INTEREST

On behalf of all authors, the corresponding author states that there is no conflict of interest.

OPEN ACCESS

REFERENCES

1. R. Schafrik and R. Sprague: *Key Eng. Mater.*, 2008, vol. 380, pp. 113–34.
2. G. McDonald and E. Carichael: *2024 global sustainability in aerospace and defense report*, Tech. rep, KPMG International, 2024.
3. L. Barbara, P. Gomez, G. Parolini, and A. de Quero: *Global aviation sustainability outlook 2025 white paper*, Tech. rep, World Economic Forum, 2025.
4. I. Lopez-Galilea, L. Hecker, A. Epishin, D. Bürger, B. Ruttert, P. Thome, S. Weber, and W. Theisen: *Metall. Mater. Trans. A*, 2023, vol. 54A(5), pp. 1509–25.
5. M. Panella, L. Zheng, M. Futoma, C. Schwalbe, D. Eyidi, P. Villechaise, and J. Cormier: Analysis of the recovery potential through repair of key tensile properties for a second generation Ni-based SX superalloys exposed to simulated routine service conditions, in: Superalloys 2024, (2024).
6. D. Reker, R. Sowa, C. Schwalbe, B. Boettger, F. Seidel, M. Panella, K. Moehwald, M. Nicolaus, and W. Tillmann: Improving repair braze gap strength through the development of a novel superalloy filler, in: Superalloys 2024, (2024).
7. S. Pahlavanyali, A. Rayment, B. Roebuck, G. Drew, and C. Rae: *Int. J. Fatigue*, 2008, vol. 30(2), pp. 397–403.
8. S. Sulzer, E. Alabort, A. Németh, B. Roebuck, and R. Reed: *Metall. Mater. Trans. A*, 2018, vol. 49, pp. 4214–35.
9. S. Korber, S. Wolff-Goodrich, R. Volkl, and U. Glatzel: *Metals*, 2022, vol. 12(7), p. 1081.
10. H. Tammpere, P. McKeown, J. Miller, C. Fang, E. Curtis, M. Gaiser-Porter, M. Burley, J. Campbell, M. Artiles, Y. Tang, S. Utada, R. Reed, and T. Clyne: *Adv. Eng. Mater.*, 2024, vol. 26(21), p. 2301073.
11. A. Girard, V. Grolleau, and D. Mohr: *Int. J. Solids Struct.*, 2025, vol. 320, p. 113527.
12. S. Soltysiak, M. Selent, S. Roth, M. Abendroth, M. Hoffmann, H. Biermann, and M. Kuna: *Mater. Sci. Eng. A*, 2014, vol. 613, pp. 259–63.
13. T. Beerli, C.C. Roth, and D. Mohr: *Acta Mater.*, 2024, vol. 263, p. 119539.
14. B. Roebuck, D.C. Cox, and R.C. Reed: An innovative device for the mechnical testing of miniature specimens of superalloys, in *Superalloys 2004*. K.A. Green, T.M. Pollock, H. Harada, T.E. Howson, R.C. Reed, J.J. Schirra, and S. Walston, eds., Metals & Materials Society, The Minerals, 2004, pp. 523–28.
15. S. Utada, R. Sasaki, R.C. Reed, and Y.T. Tang: *Metall. Mater. Trans. A*, 2023, vol. 54A(5), pp. 1549–67.
16. K.A. Christofidou, H.T. Pang, W. Li, Y. Pardhi, C.N. Jones, N.G. Jones, and H.J. Stone: Microstructural control and optimization of haynes 282 manufactured through laser powder bed fusion, in *Superalloys 2020*. S. Tin, M. Hardy, J. Clews, J. Cormier, Q. Feng, J. Marcin, C. O'Brien, and A. Suzuki, eds., Springer International Publishing, Cham, 2020, pp. 1014–23.
17. S. Perry, N. D'Souza, D. Collins, B. Roebuck, and H. Dong: *Metall. Mater. Trans. A*, 2023, vol. 54A(5), pp. 1582–96.
18. Y.T. Tang, N. D'Souza, B. Roebuck, P. Karamched, C. Panwisawas, and D.M. Collins: *Acta Mater.*, 2021, vol. 203, p. 116468.
19. S. Utada, R. Sasaki, R. Reed, and Y. Tang: *Mater. Des.*, 2022, vol. 221, p. 110911.
20. J.F.S. Markanday, N. D'Souza, N.L. Church, J.R. Miller, J.J.C. Pitchforth, L.D. Connor, S. Michalik, B. Roebuck, N.G. Jones, K.A. Christofidou, and H.J. Stone: The relationship between strain-age cracking and the evolution of γ' in laser powder-bed-fusion processed ni-based superalloys, in *Superalloys 2024*. J. Cormier, I. Edmonds, S. Forsik, P. Kontis, C. O'Connell, T. Smith, A. Suzuki, S. Tin, and J. Zhang, eds., Springer, Cham, pp. 822–35 (2024).
21. Y.T. Tang, C. Panwisawas, B.M. Jenkins, J. Liu, Z. Shen, E. Salvati, Y. Gong, J.N. Ghoussoub, S. Michalik, B. Roebuck, P.A. Bagot, S. Lozano-Perez, C.R. Grovenor, M.P. Moody, A.M. Korsunsky, D.M. Collins, and R.C. Reed: *Addit. Manuf.*, 2023, vol. 62, p. 103389.
22. Y.T. Tang, C. Schwalbe, M. Futoma, B. Roebuck, S. Utada, and R.C. Reed: *Metall. Mater. Trans. A*, 2023, vol. 54, pp. 1568–81.
23. R. Sasaki, S. Utada, Y. T. Tang, C. A. Nunes, and R. C. Reed: The effect of direct current heating on the creep behaviour of polycrystalline ni-based superalloys, in: Superalloys 2024, (2024).
24. K. Harris, G. Erickson, and R. Schwer: Mar m 247 derivations - cm 247 lc ds alloy and cmsx single crystal alloys: Properties & performance, in: Superalloys 1984, (1984).
25. B. Mansoz, L. Bortoluci Ormastroni, J. Rame, C. Schwalbe, K. Vamsi, P. Caron, J. Cormier, and F. Pettinari-Sturmel: *Intermetallics*, 2023, vol. 161, art. no. 107976.
26. M. Zupan, M.J. Hayden, C.J. Boehlert, and K.J. Hemker: *Exp. Mech.*, 2001, vol. 41, pp. 242–47.
27. J. Blaber, B. Adair, and A. Antoniou: *Exp. Mech.*, 2015, vol. 55, pp. 1105–22.
28. A. Nicolaÿ, J.-M. Franchet, N. Bozzolo, and J. Cormier: Metallurgical Analysis of Direct Aging Effect on Tensile and Creep Properties in Inconel 718 Forgings, in: J. C. J. C. Q. F. M. H. J. M. A. S. Sammy Tin, Chris O'Brien (Ed.), Superalloys2020, TMS, (2020).
29. J. Schindelin, I. Arganda-Carreras, E. Frise, V. Kaynig, M. Longair, T. Pietzsch, S. Preibisch, C. Rueden, S. Saalfeld, B. Schmid, J. Tinevez, D. White, V. Hartenstein, K. Eliceiri, P. Tomancak, and A. Cardona: *Nat. Method*, 2012, vol. 9, pp. 676–82.

30. R. J. Mitchell, M. Hardy, M. Preuss, and S. Tin: Development of γ' morphology in a P/M Rotor Disc Alloys During Heat Treatment, in: Superalloys 2004, Superalloys 2004, pp. 361–70 (2004).
31. C. Su and P. Voorhees: *Acta Mater*., 1996, vol. 44(5), pp. 1987–99.
32. S. Meher, L.K. Aagesen, L.J. Carroll, M.C. Carroll, and T.M. Pollock: *Microsc. Microanal*., 2016, vol. 22(3), pp. 1258–59.
33. R. Ricks, A. Porter, and R. Ecob: *Acta Mech*., 1983, vol. 31, pp. 43–53.
34. H. Long, H. Wei, Y. Liu, S. Mao, J. Zhang, S. Xiang, Y. Chen, W. Gui, Q. Li, Z. Zhang, and X. Han: *Acta Mater*., 2016, vol. 120, pp. 95–107.
35. M. Ignat, J.-Y. Buffiere, and J. Chaix: *Acta Metall. Mater*., 1993, vol. 41(3), pp. 855–62.
36. W. Mason: The Lüders' lines on mild steel, in: Proceedings of the Physical Society of London, Vol. 23, (1910).
37. B. Rowlands, C. Rae, and E. Galindo-Nava: *Prog. Mater. Sci*., 2023, vol. 132, p. 101038.
38. S. Oh, M. Legros, D. Kiener, and G. Dehm: *Nat. Mater*., 2009, vol. 8, pp. 95–100.
39. Y. Cui, E. Aydogan, J.G. Gigax, Y. Wang, A. Misra, S.A. Maloy, and N. Li: *Acta Mater*., 2021, vol. 202, pp. 255–65.
40. T. Smith, Y. Rao, Y. Wang, M. Ghazisaeidi, and M. Mills: *Acta Mater*., 2017, vol. 141, pp. 261–72.
41. C. Rae and R. Reed: *Acta Mater*., 2007, vol. 55(3), pp. 1067–81.
42. N. Karpstein, M. Lenz, A. Bezold, M. Wu, S. Neumeier, and E. Spiecker: *Acta Mater*., 2023, vol. 260, p. 119284.
43. A. Harte, M. Atkinson, A. Smith, C. Drouven, S. Zaefferer, J. Quinta da Fonseca, and M. Preuss: *Acta Mater*., 2020, vol. 194, pp. 257–75.